Opto-Electronic Advances

Article

May 2026, Vol. 9, No. 5

Open Access

Multistable soliton dynamics in an optical microresonator

Zichun Liao[1,2†], Yuchong Cai[1,2†], Lun Li[5], Weiqiang Wang[3,4], Shuai Li[1,2], Chi Zhang[1,2*], Wenfu Zhang[3,4*] and Xinliang Zhang[1,2*]

Abstract: Dissipative Kerr solitons (DKSs) generated in optical microresonators have shown considerable promise across multiple applications, particularly in metrology and spectroscopy. Multistable solitons enable on-chip single-cavity dual-comb generation, and can be excited via multicolor pumping in a microresonator featuring high-quality factor and strong nonlinearity, whose dispersion profile governs the soliton velocity mismatch. However, real-time characterization of complex multistable soliton dynamics remains highly challenging due to their transient nature, large bandwidth, and high repetition rate. In this work, we generate multistable soliton dynamics using a dual-pump scheme targeting distinct cavity modes and report, for the first time, their simultaneous time- and spectral-domain characterization via a chirped coherent detection scheme. These multistable solitons are measured at different carrier-envelope offset frequencies, allowing for the observation of soliton switching and annihilation processes during pump detuning. Furthermore, the gain transfer mechanisms underpinning the influence of pump detuning on soliton dynamics are investigated. This study not only deepens our understanding of complex soliton interactions within optical microresonators but also supports enhanced control and utilization of single-cavity dual-comb sources.

Keywords: microcomb; multistable soliton dynamics; coherent detection; real-time characterization

DOI: 10.29026/oea.2026.250329 | CSTR: 32247.14.oea.2026.250329

Citation: Liao ZC, Cai YC, Li L et al. Multistable soliton dynamics in an optical microresonator. *Opto-Electron Adv* **9**, 250329 (2026).

1 Introduction

Since the first microresonator-based optical frequency comb (microcombs) was realized by Del'Haye in 2007[1], considerable progress has been made in microcombs generation in recent years. Leveraging their high repetition rate, broad bandwidth, compact footprint, high coherence, and compatibility with the complementary metal oxide semiconductor (CMOS) fabrication processes, microcombs have demonstrated immense potential across diverse fields[2] such as metrology[3,4], microwave photonics[5,6], and high-speed optical communications[7]. In metrology applications, such as LiDAR ranging and interferometric spectroscopy, dual-comb systems, employing two frequency combs with a fixed repetition rate difference, have been widely adopted to enhance measurement precision and resolution. Compared to dual-comb systems based on two independent microresonators, single-cavity dual-comb sources reduce system complexity and cost and improve mutual coherence between the combs. Furthermore, in optical frequency synthesis, single-cavity dual-comb architectures combined with Kerr-induced synchronization enable efficient and stable control of optical frequency division[8]. Consequently, research on single-cavity dual-comb generation in microresonators has garnered increasing attention in recent years. Current approaches for generating dual combs in a single microresonator platform include multiplexed pumping techniques such as counter-frequency-shifted pumping[9,10], sideband-modulated pumping[11], and orthogonally polarized pumping[12,13], as well as single-pump methods based on stimulated Brillouin scattering[14]. On the other hand, while extensive research has explored diverse soliton dynamics in microresonators, including Stokes solitons[15], dark pulses[16,17],

Received: 25 November 2025
Accepted: 11 February 2026
Published online: 3 April 2026

[1]Wuhan National Laboratory for Optoelectronics & School of Optical and Electronic Information, Huazhong University of Science and Technology, Wuhan 430074, China; [2]Optics Valley Laboratory, Wuhan 430074, China; [3]State Key Laboratory of Ultrafast Optical Science and Technology, Xi'an Institute of Optics and Precision Mechanics, Chinese Academy of Sciences, Xi'an 710119, China; [4]University of Chinese Academy of Sciences, Beijing 100049, China; [5]Photonics Research Institute & Department of Electrical and Electronic Engineering, The Hong Kong Polytechnic University, Hong Kong SAR 999077, China.
† These authors contributed equally to this work.
*Correspondence: C Zhang, E-mail: chizheung@hust.edu.cn; WF Zhang, E-mail: wfuzhang@opt.ac.cn;
XL Zhang, E-mail: xlzhang@mail.hust.edu.cn

soliton crystal switching[18], breathing solitons[19], and dispersive waves[20,21], studies on direct interactions between multistable solitons excited by distinct pumps in single-cavity dual-comb systems remain limited. Investigating these multistable soliton dynamics is critical not only for advancing fundamental understanding of soliton interaction mechanisms, such as direct soliton collisions[22], but also for enabling applications like multicomb spectroscopy[11,23] and dual-comb ranging[24,25].

However, due to the ultrahigh-quality factor, strong nonlinearity, and compact size of microresonators, the characteristic timescale of soliton dynamics far exceeds the round-trip time. Additionally, microresonator solitons exhibit unique features, including high repetition rates, broad bandwidths, and ultrashort pulse durations. Real-time characterization of the complete soliton dynamics demands a detection system capable of simultaneously achieving large spectral bandwidth, high frame rates, and sub-picosecond temporal resolution over extended observation windows. This requires a system time-bandwidth product exceeding 1000[26], posing a formidable challenge. In recent years, much research has been published on capturing the soliton dynamics in microresonators[27−30]. Conventional direct detection methods[19], limited by electrical bandwidth constraints, fail to resolve combs with repetition rates beyond 50 GHz regime.

Methods of observing the transition mainly include ultrafast temporal magnifier[31] and optical sampling[29]. Nevertheless, a temporal magnifier based on parametric mixing processes introduces intensity noise during detection and lacks access to phase information and spectral evolution. In contrast, electro-optic comb coherent sampling has been used to observe the formation, collisions, breathing, Raman self-frequency shifts, and decay processes of single solitons in real time. It reveals the spectral evolution that occurs during soliton breathing[29]. Moreover, leveraging electro-optic comb coherent sampling, collision-induced rogue waves, and universal transport dynamics in chaotic Kerr microresonators have been profoundly investigated[32]. Building on this framework, the electro-optic comb coherent sampling method has been utilized to explore the dynamics of multistability in microresonators. This method has made the first observations of mutual penetration during soliton collisions and soliton bound states in multistability regimes[33,34]. However, the electro-optic comb coherent sampling necessitates a sampling comb repetition rate closely matched to the microcombs' repetition rates, and its operational bandwidth restricts the spectral characterization range. Furthermore, although the electro-optic comb-based system can reach frame rates of up to 200 MHz for high-repetition-rate microcombs, they are still unable to continuously track dynamics that extend over multiple round-trip periods. This is because such systems rely on asynchronous optical sampling, which limits each frame to capturing only one or few round-trip of soliton dynamics. Additionally, they require the soliton evolution to remain stable throughout the entire asynchronous sampling window, and an excessively high frame rate (above 20 MHz) results in a reduced signal-to-noise ratio (SNR) in measurements[32]. Recently, an innovative method that integrates artificial intelligence and linear spectral shearing interferometry (LSSI) —referred as LLSI-based intelligent single-shot full-field characterization (ISFC) —has enabled single-shot full-field characterization of femtosecond pulse trains with MHz repetition rates and low energy[35].

Here, we propose a chirped coherent detection system based on coherent detection and optical Fourier transform techniques, enabling real-time full-field characterization of spectral and temporal evolution dynamics in microresonator solitons. While coherent detection, a powerful method for extracting full-field signal information, has been widely adopted in optical communications, traditional approaches employing single-frequency continuous-wave local oscillators (LOs) suffer from limited detection bandwidth, rendering them inadequate for resolving microcomb dynamics. Previous studies (e.g., spectral segmentation[36]) attempted to expand the bandwidth but required multiple coherent receivers and complex configurations with stringent signal acquisition precision, posing significant challenges for microcomb characterization. To address bandwidth limitations, we leverage a dispersion-stretched optical Fourier transform technique. This method maps the signal spectrum under test (SUT) to a time-domain waveform with linear wavelength-to-time correspondence. By utilizing a chirped pulse, subjected to identical dispersion, as in the coherent receiver, the interference frequency between the SUT and LO remains locked at the fundamental frequency. This allows full-field spectral acquisition over 3.4 THz using a 25 GHz coherent receiver bandwidth. Subsequent digital signal processing reconstructs the real-time spectral dynamics of microcombs. Furthermore, the inverse Fourier transformation of the full-field soliton spectrum provides temporal dynamics with a time-bandwidth product of ~1800. The proposed chirped coherent detection system achieves a frame rate of 20 MHz, a spectral bandwidth of 25 nm, a spectral resolution of 28 pm, a single-frame temporal window of 520 ps, and a temporal resolution of 280 fs. Previously, we successfully applied this system to characterize multiple high-speed communication channels with diverse modulation formats[37].

In this work, multistable soliton dynamics are generated in an optical microresonator through dual-pumping of distinct longitudinal modes within the same mode family. We achieve real-time full-field characterization of these dynamics in both spectral and temporal domains using a chirped coherent detection system. Notably, leveraging the extended single-frame temporal window of the detection system, we successfully trace the soliton evolution continuously over 25 consecutive round-trips. Our measurements capture the complete temporal and spectral evolution of conventional single-soliton annihilation, as well as multistable soliton collisions, mutual penetration, and fusion, and report the first experimental observation of multistable soliton switching. By combining simulations and experimental results, we demonstrate that adjusting the pump detuning triggers transient gain transitions among multistable solitons, which in turn drive soliton switching. This offers a concrete pathway for controlling multistable microcomb states. Our findings not only deepen the fundamental understanding of multistable soliton interaction mechanisms but also enhance the flexibility of multistable microcombs, promoting their applications as integrated on-chip single-cavity dual-comb sources in dual-comb ranging, spectroscopic analysis, and optical communications.

2 Results

The high-quality factor and strong nonlinear effects of optical microresonators enable solitons to sustain their existence over an extended range, thereby facilitating the generation of multistable DKS combs via dual-pumping of resonant modes[33,34]. Moreover, the integrated dispersion of such microresonators causes mode-dependent variation in the free spectral range (FSR) within the same mode family[38]. As a result, soliton frequency combs generated by pumping resonances at different spectral positions inherently exhibit differences in their repetition rates.

As illustrated in Fig. 1, when considering only the second-order integrated dispersion of the microresonators, the FSR mismatch between two resonances with a mode number difference n is given by $\Delta FSR = n \cdot D_2/2\pi$, where D_2 is the second-order dispersion coefficient. Pumping these two resonances generates DKS combs whose repetition rate difference $\Delta f_{\rm rep}$ equals the FSR mismatch of the resonances. Consequently, the soliton pulses exhibit a stable relative velocity difference in the temporal domain, expressed as $\Delta v = \Delta f_{\rm rep} \cdot L$, where L is the cavity length. This velocity mismatch induces relative motion between coexisting solitons, leading to direct collisions that manifest in two distinct outcomes: interpenetration and fusion (partial annihilation of solitons). Furthermore, multistable solitons exhibit state-switching behavior, where abrupt transitions between soliton states alter their group velocity, generating a temporal "bending" phenomenon characterized by sudden deviations in the soliton pulse trajectory.

The state control of multistable solitons is directly governed by the detuning of the two pump lasers. Previous studies have demonstrated that the detuning difference between the two lasers critically influences the generation of multistable solitons and the switching between composite and collisional soliton states[33]. After both lasers 1 and 2 enter the red-detuned regime of the resonances to excite multistable solitons, further forward scanning of the lasers with increasing relative detuning difference causes the collision outcome between the primary and secondary soliton pulses to transition from stable interpenetration to collision-induced fusion. The cross-phase modulation interaction between the two soliton pulses establishes a refractive index barrier, acting as a temporal interaction mechanism during collisions and leading to reductions in pulse width and amplitude[22]. When the post-collision pulse width and amplitude remain above the critical threshold for soliton existence, the pulses recover their original states, exhibiting interpenetration. However, as the relative detuning of the

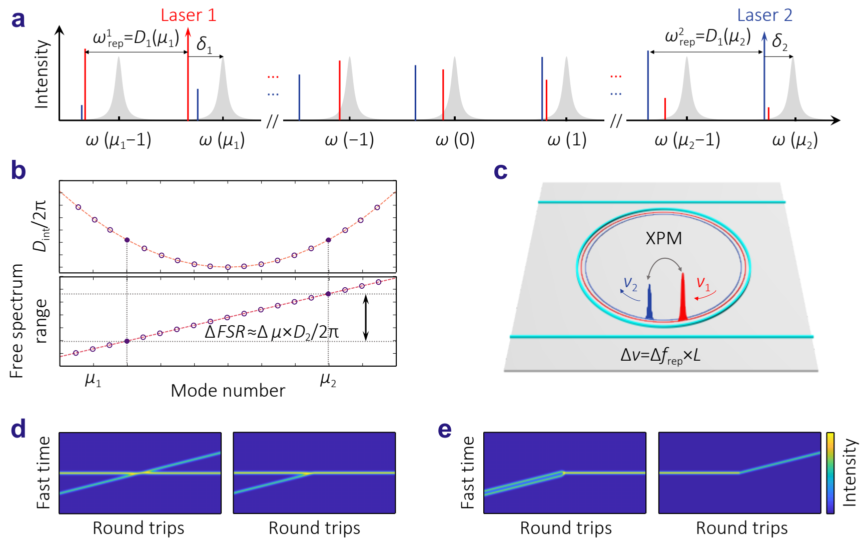

Fig. 1 | Concept of multistable soliton dynamics in a Kerr resonator. (a) Two pump lasers individually excite distinct resonances in the same mode family, generating a frequency comb whose repetition rate equals the FSR of the modes. (b) The integrated dispersion of optical microresonators induces FSR mismatches between distinct modes within the same mode family. (c) The soliton pulses' velocity difference is expressed as $\Delta v = \Delta f_{\rm rep} \cdot L$, where L is the cavity length. (d) The intensity evolutions of multistable soliton collisions. (e) The intensity evolutions of multistable soliton switching.

two lasers continues to increase, the gradual divergence in pulse width and amplitude between the primary and secondary solitons triggers symmetry breaking in collisions[39]. Specifically, if the collision-induced changes in one soliton group remain below the critical threshold while exceeding it in the other, partial annihilation occurs, manifesting as collision-induced fusion. Furthermore, the combined effect of higher-order dispersion and the relative detuning difference introduces a perturbation term $\Delta f_{D3} = \Delta\delta{\cdot}D_3/(3D_2)$ in the repetition rate difference of the multistable solitons, which likewise contributes to their state-switching dynamics. The relationship between the lasers' detuning and the soliton existence range determines the switching between multistable solitons. Physically, this switching arises from transferring pump gain between the two pump lasers.

Our approach to generating multistable soliton dynamics leverages the thermal drift of the modes. As illustrated in Fig. 2(a), Laser 1 is forward-scanned from the blue to the red-detuned side of the resonance. When Laser 1 crosses the resonance center and enters the red-detuned regime to excite solitons, the coupled intracavity power drops abruptly, inducing a rapid temperature decrease. This thermal contraction causes a global blue shift of the mode family, effectively equivalent to a cold-cavity configuration where Laser 2, initially positioned on the blue-detuned side of the resonance, undergoes forward scanning. As Laser 1 continues its forward scan, Laser 2 passively enters the red-detuned region, exciting secondary solitons and generating multistable solitons. Critical to this process is the precise adjustment of the initial detuning of Laser 2. If the detuning is too large, Laser 2 cannot passively enter the red-detuned region to generate secondary solitons; conversely, if it is too small, Laser 2 prematurely enters the red-detuned regime, causing both pumps to transition abruptly from the modulation instability state to a single-frequency state. Additionally, backward Rayleigh scattering within the microresonator generates reflected counter-propagating fields for the clockwise and counterclockwise pump lasers, as well as their soliton fields[40]. Ultimately, the multistable solitons are output unidirectionally from the microresonator.

Although the temporal structure of the intracavity field is at the sub-picosecond timescale, the transition dynamics are described at a much longer timescale, which is correlated with the cavity photon time of the microresonator. The difference between the two dimensions in the timescale results in a challenge for obtaining a comprehensive full-field result for the dynamics. To realize coherent detection of a large bandwidth, we decide to transform the detection from the temporal domain to the spectral domain[41], which means that a chirped pulse serves as the LO of the system, and the intracavity soliton field possesses the same chirp. Dispersion stretching maps the signal's spectrum into the time domain, establishing a linear time-frequency mapping relationship. However, the high-repetition-rate of microcombs introduces severe aliasing in the dispersion-stretched time-domain spectrum, making direct detection infeasible. To address this, we utilize a chirped LO pulse that undergoes identical dispersion stretching. Through chirped coherent detection, both the intensity and phase of the time-mapped spectrum of the signal are captured. Full-field soliton information is then processed in the digital domain,

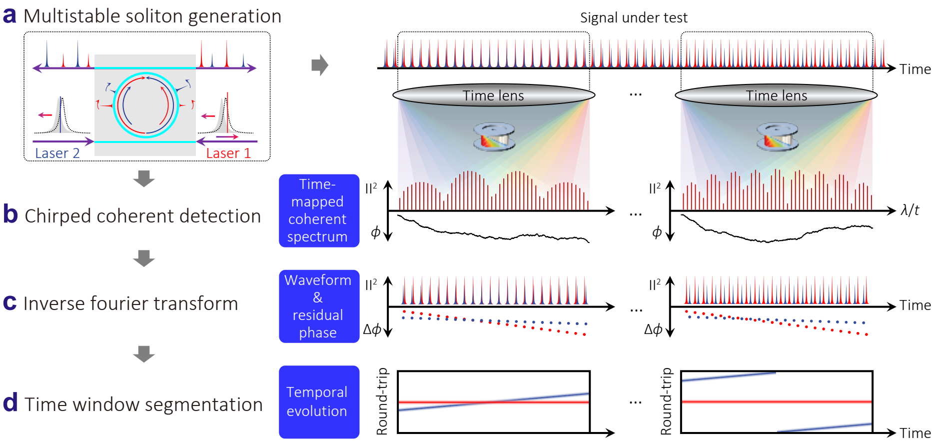

Fig. 2 | Generation of multistable soliton dynamics and the observation process of soliton dynamics. (a) Dual-pump-based multistable soliton generation. Two pump lasers excite distinct resonances within the same mode family to generate multistable solitons. Rayleigh backscattering within the microresonator enables unidirectional output of multistable solitons from a single port [40]. (b) Chirped coherent detection to obtain the time-mapped coherent spectrum. Detailed configurations can be found in Supplementary Section 2. By acquiring different frequency bands in a time-division manner, the coherent detection bandwidth is increased to 3.4 THz[37]. (c) Retrieve the real-time waveform via the inverse Fourier transform. Within each 520 ps time window per frame, over 25 round-trip real-time soliton dynamics can be continuously observed. Additionally, the residual phase at each soliton peak can serve as a basis for monitoring the carrier-envelope offset frequencies. (d) The continuous temporal waveforms are segmented into a temporal evolution based on the soliton round-trip time.

where phase compensation is applied to remove the chirp and spectral aliasing induced by dispersion stretching. This procedure recovers the full-field spectrum of the signal, as shown in Fig. 2(b). Leveraging the ability of chirped coherent detection to acquire the full-field time-mapped spectrum, digital phase compensation effectively replaces the quadratic phase modulation typically required in conventional time-lens. This enables accurate characterization of the full-field signal spectrum. Next, an inverse Fourier transform is applied to reconstruct the temporal waveform and phase of the signal, as shown in Fig. 2(c). Finally, the continuous temporal waveforms are segmented and reassembled according to the soliton round-trip time, yielding the 2D evolution portraits shown in Fig. 2(d). The Methods and Supplementary Section 2 will present a detailed theoretical framework for this method.

To characterize the test capability of the system, firstly, we generate stable single and doublet solitons for full-field characterization. As shown in Fig. 3(a), the red curve represents the reference spectrum measured by an optical spectrum analyzer (AQ6319, YOKOGAWA), which deviates from the conventional single-soliton envelope due to the spectral amplification profile imposed by the Erbium-doped fiber amplifier on the amplified soliton. The blue curve, obtained from the chirped coherent detection system, exhibits excellent agreement with the OSA-measured spectral envelope, with comb teeth positions aligning precisely. The blue curve represents a measurement bandwidth of 25 nm, which is consistent with the theoretical detection limit of the system. In Fig. 3(b), intensity fluctuations in the pulse train measured within a single temporal window arise from the envelope distortion introduced by the electrical amplifier in the coherent receiver. The single-frame temporal window length is measured as 520 ps, matching the system specifications. The black curve represents the corresponding phase, which remains smooth throughout the pulse duration, in agreement with theoretical predictions. The red data points represent the residual phase of the soliton pulses, reflecting the difference between the center frequencies of the soliton and the LO. Fig. 3(c) shows a microcomb repetition period of 20.39 ps, corresponding to a repetition rate of 49.04 GHz, closely matching the theoretical value of 49 GHz, thereby verifying the system's temporal accuracy. Fig. 3(d) shows the system temporal resolution of about ~0.3 ps. Similarly, Fig. 3(e–h) present the full-field characterization results for stable doublet solitons. Notably, the residual phase profiles of the doublet solitons generated by the same pump laser exhibit nearly identical temporal variation rates, indicating an identical offset between their center frequencies and that of the LO. These results confirm that the system's temporal

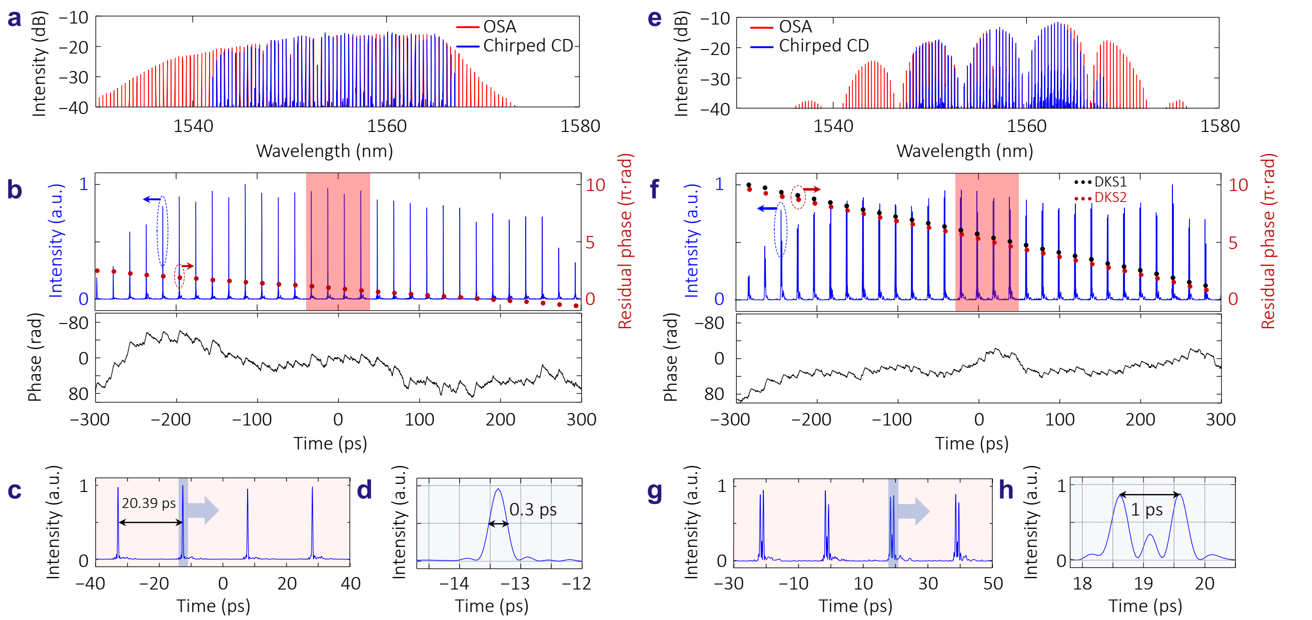

Fig. 3 | Observing stable soliton states with the proposed system. (a) The spectrum of a stable singlet soliton state detected by an optical spectrum analyzer (OSA, red curve) and the chirped coherent detection (CD, blue curve). (b) A frame of a stable singlet soliton state observed by the proposed system. The blue curve is the intensity of the temporal waveform, and the black curve is the phase of the temporal waveform. The red data points represent the residual phase of the temporal waveform, which originates from the temporal phase at the peak of the soliton pulse. (c) The zoom-in version of (b). The pulse spacing is 20.39 ps at the time scale. (d) The zoom-in version of (c). The single pulse with a FWHM of 300 fs. (e) The spectrum of a stable doublet soliton state detected by an OSA (red curve) and the chirped CD (blue curve). (f) A frame of a stable doublet singlet soliton state observed by the proposed system. The blue curve is the intensity of the temporal waveform, and the red curve is the phase of the temporal waveform. The red and black data points represent the residual phases of the two soliton groups in the time domain, respectively. (g) The zoom-in version of (f). (h) The zoom-in version of (g). The delay difference between the doublet solitons is 1 ps.

resolution and spectral bandwidth are sufficient for characterizing soliton dynamics.

To validate whether the chirped coherent detection system meets the requirements for soliton dynamic evolution measurements, the two pump lasers are set to a power of 2 W with an initial detuning difference of 260 MHz. During the forward frequency scanning of Laser 1 from the blue-detuned to the red-detuned side of the resonance, Laser 2 remains in the blue-detuned regime, thus generating only monostable soliton dynamics. Fig. 4(a) reveals that the monostable soliton pulses share identical group velocities, with stable pulses' spacing. As the detuning increases, the solitons undergo spontaneous annihilation. The corresponding spectral evolution in Fig. 4(b) shows that the spacing of the pulses remains stable, while the spectral envelope undergoes variation only during soliton extinction. Fig. 4(c) highlights specific single-frame snapshots (Fig. 4(d) ①–④), corresponding to states with five, four, three, and singlet solitons, respectively. The residual phases of the soliton pulses in these frames are shown in Fig. 4(d). Notably, the residual phase slopes of both multi-soliton and singlet soliton states exhibit high similarity, reflecting their consistent center frequencies relative to the LO. The accurate full-field characterization of monostable soliton evolution confirms that the chirped coherent detection system achieves sufficient frame rates and single-frame temporal window lengths to resolve soliton dynamics.

Subsequently, we investigate the multistable soliton collision dynamics through numerical simulations and experimental observations. In simulations, when both lasers enter the red-detuned regime within the soliton existence range, they excite multistable solitons. As shown in Fig. 5(a), due to the integrated dispersion, a stable velocity difference and repetition rate mismatch arise between the two soliton groups, leading to periodic interpenetration collisions. Correspondingly, the spectral envelope undergoes periodic density variations as the pulses' spacing changes, accompanied by localized power dips at collision instants. Experimental observations of soliton power and temporal-spectral evolution exhibit excellent agreement with these simulated phenomena. In the experiment, Lasers 1 and 2 are separated by 7 FSRs. Based on the microresonator dispersion parameters, the theoretical repetition rate difference between the two soliton groups, derived by neglecting higher-order dispersion, is 457.38 kHz. In contrast, the experimentally characterized collision frequency of the multistable solitons is measured as 454.55 kHz, as illustrated in Fig. 5(b). The close agreement between these values confirms the successful generation of multistable solitons. Furthermore, as shown in Fig. 5(c), the residual phases of the primary and secondary solitons reveal center frequency differences relative to the LO of 8.77 GHz and 3.95 GHz, respectively. This

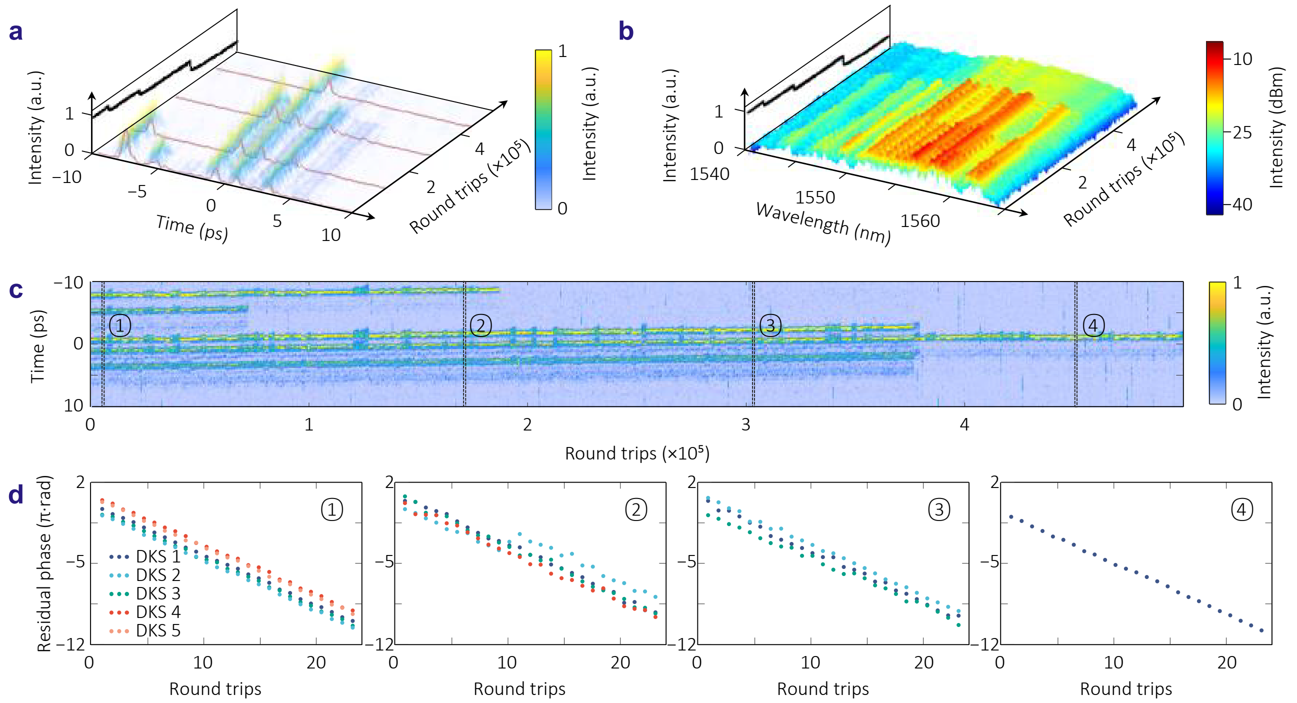

Fig. 4 | Observing the evolution of the monostable soliton dynamics. (a) Temporal waveform evolution during the transition from a five-soliton state to a singlet soliton state. The process exhibits a stepwise reduction in soliton number (5→4→3→1). The black solid line on the left marks the soliton power steps, which descend as the number decreases. (b) Corresponding spectral evolution of the dynamic process in (a). As the soliton number decreases, the spectral envelope transitions from a densely packed structure to a sparser configuration. (c) The 2D evolution portrait of (a). (d) ①–④ display the residual phase of the soliton pulses for the corresponding single-frame temporal windows in (c).

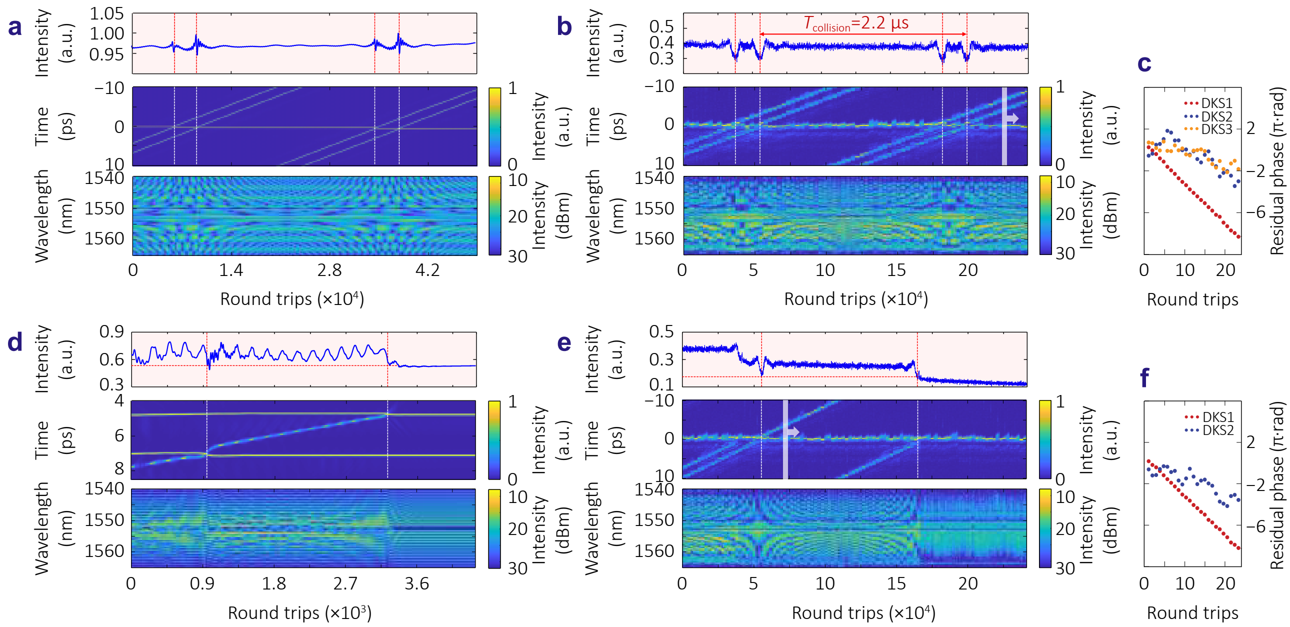

Fig. 5 | Numerical simulations and experimental observations of multistable soliton collision dynamics. (a) Numerical simulation of soliton interpenetration. From top to bottom: soliton power trace, 2D temporal evolution portrait, and 2D spectral evolution portrait. The *x*-axis in both 2D portraits represents the slow time (in units of round-trip number). The *y*-axis of the temporal map corresponds to the fast time (full scale is one round-trip time), while the spectral portrait's *y*-axis spans the wavelength range. (b) Experimental observation of soliton interpenetration. The collision period is 2.2 μs, corresponding to a collision frequency of 454.55 kHz. (c) Residual phase evolution of multistable solitons in a specific single-frame window from (b). Here, DKS 1 denotes the primary soliton, while DKS 2 and DKS 3 represent secondary solitons. (d) Numerical simulation of soliton collision-induced fusion. The soliton power exhibits a dip at the collision point, with the dip magnitude matching the post-fusion power level. (e) Experimental observation of soliton collision-induced fusion. (f) Residual phase evolution of multistable solitons in a specific single-frame window from (e).

indicates that their respective pump lasers independently govern the center frequencies of multistable solitons. The interpenetration phenomenon observed here aligns with prior studies on multistable soliton collisions in microresonators[33].

Furthermore, we observe collision-induced fusion phenomena. As shown in Fig. 5(d, e), both interpenetration and fusion events exhibit power dips in the experimental traces, with the dip minima matching the power level of the subsequent soliton step, consistent with numerical simulations of collision-induced fusion. Prior studies on generalized soliton collisions suggest that interpenetration corresponds to temporary annihilation and recovery of colliding pulses, while fusion involves permanent annihilation of one soliton group[22]. Our results strongly corroborate these conclusions. The residual phases of fused and mutually penetrated solitons exhibit similar characteristics, as shown in Fig. 5(f). Here, DKS 1 and DKS 2 display center frequency differences relative to the LO of 8.64 GHz and 3.44 GHz, respectively, demonstrating their respective pump lasers' independent control of soliton center frequencies.

Beyond multistable soliton collisions, we also discover a transient switching phenomenon between soliton groups, which represents a novel finding in the field of microresonator soliton dynamics. Simulations demonstrate that the occurrence of multistable soliton switching is directly governed by whether the pump detunings lie within the soliton existence range. The soliton existence ranges $\left(\frac{\sqrt{3}}{2}\kappa \le \delta_{\text{DKS}} \le \frac{\pi^2 f^2}{16}\kappa\right)$ for both pump lasers align with the theoretical predictions in ref.[42], where *f* denotes the normalized pump power. As shown in Fig. 6(a), when Laser 2 operates outside the soliton existence range and Laser 1 is forward-scanned beyond its soliton existence range, the primary soliton annihilates due to insufficient pump gain. The corresponding experimental observation of single-soliton annihilation is presented in Fig. 6(d). In contrast, when Laser 2 remains within the soliton existence range, Laser 1 exits its range, the primary soliton annihilates and switches to the secondary soliton state. This switching alters the soliton's repetition rate and group velocity, manifesting as a temporal "bending" of the pulse trajectory, as shown in Fig. 6(b) and experimentally observed in Fig. 6(e). Following the switch, the secondary soliton ceases to move relative to other solitons, thereby stabilizing the pulse spacing and spectral envelope. These observations suggest a pump gain transition mechanism under dual-pump conditions, where soliton states switch as pump gain redistributes between the two pumps. Furthermore, we identify an additional switching mechanism: collision-induced switching. Previous studies show that colliding solitons from the same pump may merge into a high-energy state before annihilating[33]. Intriguingly,

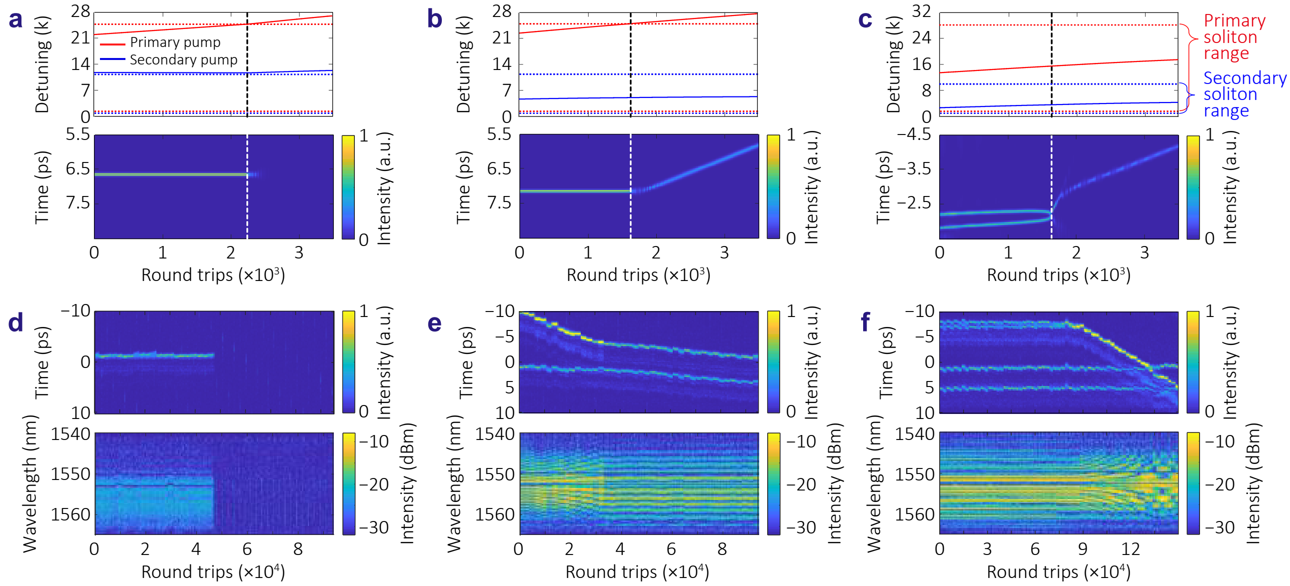

Fig. 6 | Numerical simulations and experimental observations of multistable soliton switching. (a–c) Numerical simulation results for a monostable soliton annihilation. (b) Multistable soliton self-switching, and (c) multistable soliton collision-induced switching. Top panels: detuning evolution of the two pump lasers. Red and blue dashed lines mark the effective existence boundaries of the primary and secondary solitons, respectively. Bottom panels: 2D temporal evolution portraits of soliton dynamics. (d–f) Experimental observations corresponding to (d) monostable soliton annihilation. (e) Multistable soliton self-switching, and (f) multistable soliton collision-induced switching. Top panels: 2D temporal evolution portraits of soliton dynamics. Bottom panels: corresponding 2D spectral evolution portraits.

when Laser 2 remains within the soliton existence range, colliding primary solitons transform into secondary solitons instead of annihilating. This collision-induced switching is validated by both simulations and experiments, as shown in Fig. 6(c) and 6(f), respectively. Both self-switching and collision-induced switching originate from the pump gain transition mechanism. Such mechanisms have been extensively studied in orthogonally pumped fiber ring cavities[43], where modulating pump field strengths achieve soliton switching. In this work, the gradual reduction of coupled power into the mode, resulting from the forward detuning scanning of Laser 1, directly drives the pump gain transition[44].

3 Discussion

In summary, we generate multistable soliton dynamics with stable velocity and repetition rate differences by pumping distinct longitudinal modes using dual pump lasers, and perform real-time full-field characterization via a chirped coherent detection system. By observing stationary singlet and doublet solitons, we confirm that the system's resolution, single-frame temporal window, spectral bandwidth, and phase-resolving capability are well-suited for soliton characterization. The system's frame rate, validated by monitoring monostable soliton annihilation during forward pump detuning scans, is sufficient to resolve soliton dynamic evolution. Although the current temporal resolution is limited to 0.3 ps, it can be improved by employing a broader-bandwidth LO at the expense of reduced frame rates. Similarly, higher-bandwidth coherent receivers could extend the temporal recording length, suggesting a viable pathway for optimizing the system's time-bandwidth product. Through coupled Lugiato-Lefever equation simulations, we successfully reproduce the generation, collisions, and switching of multistable solitons, all of which are experimentally observed using a chirped coherent detection system. Our findings reveal that soliton annihilation occurs instantaneously during collisions: interpenetration corresponds to transient annihilation followed by recovery, while collision-induced fusion constitutes permanent annihilation. Finally, the observation of multistable soliton switching in both simulations and experiments unveils a pump gain transition mechanism, demonstrating that controlled soliton switching can be achieved by tuning pump detuning.

Notably, the chirped coherent detection system overcomes critical limitations in current microcomb dynamic characterization techniques, including limited bandwidth in direct detection, the absence of phase information in time-lens amplification, and discontinuous sampling in coherent comb-based techniques. By integrating optical Fourier transform with chirped coherent reception, the system enables real-time and continuous acquisition of both intensity and phase across a broad spectral range. In contrast to mainstream techniques, it uniquely provides simultaneous spectral and temporal phase-intensity profiles, achieving a 3.4 THz optical bandwidth detection with only a 25 GHz electronic receiver bandwidth. Furthermore, the system concurrently delivers high frame rates, high spatiotemporal resolution, and continuous monitoring of the transient process. This work validates the system's robust capabilities for characterizing high-speed microresonator soliton dynamics and underscores its broad application potential, including in ultrafast terahertz signal measurements in optical carriers.

Our study deepens the understanding of multistable soliton interaction mechanisms and offers concrete pathways for controlling both multistable and monostable soliton states. In metrological applications such as dual-comb ranging and spectroscopic analysis, as well as in wavelength-division multiplexed communication systems, the capability to precisely tune soliton states through pump detuning, utilizing mode-selective repetition rate differences, significantly enhances the adaptability and utility of multistable microcombs in complex scenarios.

4 Methods

Numerical simulations: based on the coupled Lugiato-Lefever equations with a cavity thermal effect[10,33,45]

$$T_{\mathrm{R}}\frac{\partial E_1}{\partial t}=\left[-\mathrm{i}(\delta_1-\delta_{\mathrm{thermal}})-\frac{\alpha}{2}+\mathrm{i}L\sum_{k\geq 2}\frac{\beta_k}{k!}\left(\mathrm{i}\frac{\partial}{\partial\tau}\right)^k+\mathrm{i}\gamma L\left(|E_1|^2+2|E_2|^2\right)\right]E_1+\sqrt{\theta P_1^{\mathrm{in}}}\ , \quad (1)$$

$$T_{\mathrm{R}}\frac{\partial E_2}{\partial t}=\left[-\mathrm{i}(\delta_2-\delta_{\mathrm{thermal}})-\frac{\alpha}{2}+\mathrm{i}L\sum_{k\geq 2}\frac{\beta_k}{k!}\left(\mathrm{i}\frac{\partial}{\partial\tau}\right)^k+\mathrm{i}\gamma L\left(|E_2|^2+2|E_1|^2\right)\right]E_2+\sqrt{\theta P_2^{\mathrm{in}}}\cdot\mathrm{e}^{-\mathrm{i}\Delta w\tau}\ , \quad (2)$$

$$\frac{\partial\delta_{\mathrm{thermal}}}{\partial t}=\frac{1}{C_{\mathrm{p}}}\left[K_1\left(|E_1|^2+|E_2|^2\right)-K\delta_{\mathrm{thermal}}\right]\ , \quad (3)$$

where E_1 and E_2 are the intracavity fields of the primary and the secondary solitons, respectively, $T_{\mathrm{R}}$is the round-trip time, t is the slow time, τ is the fast time, $\delta_{1,2}$ is the detuning of the pump laser, $\delta_{\mathrm{thermal}}$ is the thermal detuning shift, α is the total decay per roundtrip, β_k is the k-th order dispersion, γ is the nonlinear coefficient, L is the cavity length, θ is the coupling rate from the bus waveguide to the resonator, $P^{\mathrm{in}}{}_{1,2}$ is the power of the pump laser, $\Delta\omega = 2\pi FSR(\mu_2 - \mu_1)$ is the frequency offset between the lasers' modes. Equation (3) describes the thermal dynamics in the resonator, where C_{p} is the thermal capacity (J/°C), K is the thermal conductivity (J/s/°C), and K_1 is the effective thermal detuning coefficient (/°C)[45,46]. The simulations focus on the co-propagating multistable soliton dynamics driven by Lasers 1 and 2. Under the practical bidirectional pumping configuration, the pump powers are set to 2.5 W (Laser 1) and 0.9 W (Laser 2), respectively, with only cross-phase modulation considered between the multistable soliton fields.

4.1 Soliton generation

The experiment generates multistable soliton dynamics by pumping two distinct modes within the same fundamental mode family using dual pump lasers. The dual-pump-based soliton generation setup is illustrated in Fig. S1. Laser 1 (TLB-6700, New Focus) and 2 (BASIK E15, NKT Photonics), operating at wavelengths of 1553 nm and 1549.9 nm, respectively, are amplified by an Erbium-doped fiber amplifier and coupled into the microresonator. Both Lasers are polarized to align with the transverse magnetic (TM) mode, which exhibits an FSR of 49 GHz and a second-order dispersion parameter $D_2/2\pi$ = 65.34 kHz at the reference mode. It is noteworthy that all pumped cavity modes are found within the anomalous dispersion regime. The pump lasers are separated by 7 FSRs, resulting in a theoretical repetition rate difference of 457.38 kHz between the two soliton frequency combs. The relative detuning and pump powers of Lasers 1 and 2 are optimized to achieve multistable soliton dynamics. First, the microresonator is cooled using a thermoelectric controller to blue-shift the mode family. A vector network analyzer monitors the relative detuning difference between the pump lasers. The detuning of Pump 1 is dynamically controlled by adjusting the piezoelectric transducer bias voltage via an arbitrary waveform generator. Specifically, Laser 1 is backward-scanned by 250 MHz over 1 ms, followed by a forward scan of 1000 MHz over 3 ms. During the forward scan, the system enters the soliton state into the red-detuned regime, generating characteristic soliton power steps.

4.2 Chirped coherent detection

As illustrated in Fig. S2, the measurement setup comprises a microresonator soliton generation module with a reference and a chirped coherent detection system. The LO is a homemade mode-locked fiber laser with an FSR of 20 MHz. This Laser is passed through a dispersion compensation fiber (DCF) with a dispersion of approximately 2120 ps^2, generating a chirped pulse source. The SUT from the microresonator is transmitted through another DCF with nearly identical dispersion to the LO's DCF, enabling an optical Fourier transform to map the spectrum into a time-domain waveform with a linear wavelength-to-time relationship. To suppress pump power that could saturate the coherent receiver, fiber Bragg gratings filter out Laser 1 (wavelength: 1553 nm) and Laser 2 (wavelength: 1549.9 nm). Additionally, a continuous-wave laser at 1542 nm is a reference wavelength to calibrate the SUT's detection spectrum, which is filtered out during digital signal processing. The frequency-mapped SUT and reference continuous-wave signals are then fed into the signal port of a coherent receiver with a bandwidth of 25 GHz. The other port of the coherent receiver is connected to the stretched LO, ensuring that the hybrid frequency between the LO and SUT remains at the fundamental frequency within the receiver's operational bandwidth. Consequently, the system achieves a detection bandwidth equivalent to the LO's filtering bandwidth (~25 nm), corresponding to a temporal resolution of ~300 ps. With a frame rate of 20 MHz and a single-frame recording length of 520 ps, the system can continuously capture full-field dynamic evolution over 25 round-trips within a single frame. By stitching multiple frames, the complete soliton dynamics are reconstructed. As long as the soliton evolution speed is significantly slower than the system frame rate, the system reliably captures critical dynamic information. Additionally, Table 1 lists and compares the performance metrics of various microcomb detection techniques, including chirped coherent detection. Overall, chirped coherent detection offers significant advantages when all indicators are taken into account.

Table 1 | Comparison of various microcomb detection technologies.

Methods	Full-field Waveform	Spectrometer	Time resolution (ps)	Frame rate (MHz)	Single-shot record length (ps)
Direct detection[19]	×	×	8	NA	NA
FROG[35]	√	√	0.002	1.43×10^{-7}	30
SPIDER[47]	√	√	0.2	NA	4
Temporal magnifier[21,31]	×	×	0.6	25	190
EO comb sampling[29]	√	√	0.55	20–100	20
LLSI-based ISFC[35]	√	√	0.008	0.414–1	37
Chirped coherent detection[37]	√	√	0.28	20	520

References

1. Del'Haye P, Schliesser A, Arcizet O et al. Optical frequency comb generation from a monolithic microresonator. *Nature* **450**, 1214–1217 (2007).
2. Kippenberg TJ, Gaeta AL, Lipson M et al. Dissipative Kerr solitons in optical microresonators. *Science* **361**, eaan8083 (2018).
3. Trocha P, Karpov M, Ganin D et al. Ultrafast optical ranging using microresonator soliton frequency combs. *Science* **359**, 887–891 (2018).
4. Suh MG, Yang QF, Yang KY et al. Microresonator soliton dual-comb spectroscopy. *Science* **354**, 600–603 (2016).
5. Liang W, Eliyahu D, Ilchenko VS et al. High spectral purity Kerr frequency comb radio frequency photonic oscillator. *Nat Commun* **6**, 7957 (2015).
6. Newman ZL, Maurice V, Drake T et al. Architecture for the photonic integration of an optical atomic clock. *Optica* **6**, 680–685 (2019).
7. Marin-Palomo P, Kemal JN, Karpov M et al. Microresonator-based solitons for massively parallel coherent optical communications. *Nature* **546**, 274–279 (2017).
8. Moille G, Shandilya P, Niang A et al. Versatile optical frequency division with Kerr-induced synchronization at tunable microcomb synthetic dispersive waves. *Nat Photonics* **19**, 36–43 (2025).
9. Yang QF, Yi X, Yang KY et al. Counter-propagating solitons in microresonators. *Nat Photonics* **11**, 560–564 (2017).
10. Wang ZH, Wang YF, Shi BQ et al. Rhythmic soliton interactions for integrated dual-microcomb spectroscopy. *Phys Rev X* **15**, 011061 (2025).
11. Lucas E, Lihachev G, Bouchand R et al. Spatial multiplexing of soliton microcombs. *Nat Photonics* **12**, 699–705 (2018).
12. Wang WQ, Zhang WF, Lu ZZ et al. Self-locked orthogonal polarized dual comb in a microresonator. *Photonics Res* **6**, 363–367 (2018).
13. Bao CJ, Liao PC, Kordts A et al. Orthogonally polarized frequency comb generation from a Kerr comb via cross-phase modulation. *Opt Lett* **44**, 1472–1475 (2019).
14. Zhang H, Tan T, Chen HJ et al. Soliton microcombs multiplexing using intracavity-stimulated brillouin lasers. *Phys Rev Lett* **130**, 153802 (2023).
15. Yang QF, Yi X, Yang KY et al. Stokes solitons in optical microcavities. *Nat Phys* **13**, 53–57 (2017).
16. Nazemosadat E, Fülöp A, Helgason ÓB et al. Switching dynamics of dark-pulse Kerr frequency comb states in optical microresonators. *Phys Rev A* **103**, 013513 (2021).
17. Xue XX, Xuan Y, Liu Y et al. Mode-locked dark pulse Kerr combs in normal-dispersion microresonators. *Nat Photonics* **9**, 594–600 (2015).
18. Cole DC, Lamb ES, Del'Haye P et al. Soliton crystals in Kerr resonators. *Nat Photonics* **11**, 671–676 (2017).
19. Lucas E, Karpov M, Guo H et al. Breathing dissipative solitons in optical microresonators. *Nat Commun* **8**, 736 (2017).
20. Yi X, Yang QF, Zhang XY et al. Single-mode dispersive waves and soliton microcomb dynamics. *Nat Commun* **8**, 14869 (2017).
21. Li YN, Huang SW, Li BW et al. Real-time transition dynamics and stability of chip-scale dispersion-managed frequency microcombs. *Light Sci Appl* **9**, 52 (2020).
22. Descalzi O, Cisternas J, Escaff D et al. Noise induces partial annihilation of colliding dissipative solitons. *Phys Rev Lett* **102**, 188302 (2009).
23. Yang QF, Shen BQ, Wang HM et al. Vernier spectrometer using counterpropagating soliton microcombs. *Science* **363**, 965–968 (2019).
24. Suh MG, Vahala KJ. Soliton microcomb range measurement. *Science* **359**, 884–887 (2018).
25. Wang ZH, Wang YF, Shi BQ et al. Nanometric dual-comb ranging

using photon-level microcavity solitons. *Nat Commun* **16**, 6853 (2025).

26. Raja AS, Voloshin AS, Guo HR et al. Electrically pumped photonic integrated soliton microcomb. *Nat Commun* **10**, 680 (2019).
27. Nie MM, Li BW, Jia KP et al. Dissipative soliton generation and real-time dynamics in microresonator-filtered fiber lasers. *Light Sci Appl* **11**, 296 (2022).
28. Goda K, Jalali B. Dispersive Fourier transformation for fast continuous single-shot measurements. *Nat Photonics* **7**, 102–112 (2013).
29. Yi X, Yang QF, Yang KY et al. Imaging soliton dynamics in optical microcavities. *Nat Commun* **9**, 3565 (2018).
30. Herink G, Jalali B, Ropers C et al. Resolving the build-up of femtosecond mode-locking with single-shot spectroscopy at 90 MHz frame rate. *Nat Photonics* **10**, 321–326 (2016).
31. Li BW, Huang SW, Li YN et al. Panoramic-reconstruction temporal imaging for seamless measurements of slowly-evolved femtosecond pulse dynamics. *Nat Commun* **8**, 61 (2017).
32. Wang Z, Zhu KX, Zhang FX et al. Collision-induced rogue waves and universal transport dynamics in chaotic Kerr microresonators. *Sci Adv* **11**, eadv9422 (2025).
33. Weng WL, Bouchand R, Kippenberg TJ. Formation and collision of multistability-enabled composite dissipative Kerr solitons. *Phys Rev X* **10**, 021017 (2020).
34. Weng WL, Bouchand R, Lucas E et al. Heteronuclear soliton molecules in optical microresonators. *Nat Commun* **11**, 2402 (2020).
35. Pu GQ, Luo C, Hu WS et al. Intelligent single-shot full-field characterization over femtosecond pulses. *Nat Commun* **16**, 11621 (2025).
36. Fontaine NK, Scott RP, Zhou LJ et al. Real-time full-field arbitrary optical waveform measurement. *Nat Photonics* **4**, 248–254 (2010).
37. Li L, Zhang C, Cai YC et al. Real-time Fourier-domain optical vector oscilloscope. *Sci Adv* **9**, eadg2538 (2023).
38. Fujii S, Tanabe T. Dispersion engineering and measurement of whispering gallery mode microresonator for Kerr frequency comb generation. *Nanophotonics* **9**, 1087–1104 (2020).
39. Yi X, Yang QF, Yang KY et al. Soliton frequency comb at microwave rates in a high-*Q* silica microresonator. *Optica* **2**, 1078–1085 (2015).
40. Wang XY, Xie P, Wang Y et al. Experimental demonstration of self-oscillation microcomb in a mode-splitting microresonator. *Front Phys* **10**, 908141 (2022).
41. Li AL, Xu BL, Fu CS et al. Ultrafast single-shot optical vector network analyzer based on coherent time-stretch. *APL Photonics* **5**, 106109 (2020).
42. Herr T, Brasch V, Jost JD et al. Temporal solitons in optical microresonators. *Nat Photonics* **8**, 145–152 (2014).
43. Xu G, Nielsen AU, Garbin B et al. Spontaneous symmetry breaking of dissipative optical solitons in a two-component Kerr resonator. *Nat Commun* **12**, 4023 (2021).
44. Del Bino L, Silver JM, Stebbings SL et al. Symmetry breaking of counter-propagating light in a nonlinear resonator. *Sci Rep* **7**, 43142 (2017).
45. Zhou H, Geng Y, Cui WW et al. Soliton bursts and deterministic dissipative Kerr soliton generation in auxiliary-assisted microcavities. *Light Sci Appl* **8**, 50 (2019).
46. Guo H, Karpov M, Lucas E et al. Universal dynamics and deterministic switching of dissipative Kerr solitons in optical microresonators. *Nat Phys* **13**, 94–102 (2017).
47. Iaconis C, Walmsley IA. Spectral phase interferometry for direct electric-field reconstruction of ultrashort optical pulses. *Opt Lett* **23**, 792–794 (1998).

Acknowledgements

We acknowledge partial funding support from the National Natural Science Foundation of China under Grants U25D8011 and 62075238, in part by the Hubei Provincial Natural Science Foundation of China under Grant 2025AFA109, and in part by the Innovation Project of Optics Valley Laboratory under Grant OVL2024BB028.

Author contributions

Z.L., Y.C., and C.Z. proposed the technique and planned the experimental design. Z.L. and L.L. set up the chirped coherent detection system. W.Z. and W.W. fabricate the microcomb chip, and Z.L. and S.L. simulate the soliton dynamics and generate the soliton. C.Z., W.Z., and X.Z. supervised measurements and analysis. All authors wrote, discussed, and revised the manuscript.

Competing interests

The authors declare no competing financial interests.

Open Access This article is licensed under a Creative Commons Attribution 4.0 International License, which permits use, sharing, adaptation, distribution and reproduction in any medium or format, as long as you give appropriate credit to the original author(s) and the source, provide a link to the Creative Commons license, and indicate if changes were made. To view a copy of this license, visit http://creativecommons.org/licenses/by/4.0/

©The Author(s) 2026.

Published by Editorial Office of *Opto-Electronic Advance*, Institute of Optics and Electronics, Chinese Academy of Sciences.

Opto-Electronic Journals Group
www.oejournal.org

Scan for Article PDF